Polarimetric Airborne Radar Sounding as an Approach to Characterizing Subglacial Röthlisberger Channels

Kirk M. Scanlan, Dillon P. Buhl, *Member, IEEE*, and Donald D. Blankenship

***Abstract*—Conventional airborne radar sounding techniques are well suited to the detection and characterization of flat-lying, specular subglacial water bodies. However, topographically positive, diffusively scattering Röthlisberger (R-) channels are more difficult to image, while also exerting substantial control on basal friction and ice dynamics. As subglacial R-channels share geometrical similarities with targets of interest in polarimetric ground-penetrating radar studies (i.e., cylindrical pipes), in this article, we investigate whether similar concepts can be adapted to detect and characterize R-channels. While closed-form analytical solutions exist for the scattering widths (SWs) of perfect electrically conducting and dielectric circular cylinders, the insight they provide for the polarimetric response of half-cylinder R-channels is limited. As such, a series of modeling experiments have been performed to characterize the SWs of half cylinders. Our results demonstrate that scattering from subglacial R-channels depends on numerous factors including the polarization and frequency of the incident radar wave, the size of the R-channel, and the relative orientation of the R-channel to a pair of orthogonally oriented, linearly polarized radar antennas. The results imply that patterns in the like-polarized echo powers across the signal bandwidth may be useful in inferring R-channel existence and possibly estimate R-channel size. However, as differences in SW are small and decrease with increasing misalignment between the acquisition system antennas and R-channel strike, achieving a high degree of radiometric resolution and stability should be a driving factor in polarimetric radar system design.**

***Index Terms*—Airborne radar, cryosphere, radar cross-sections, radar polarimetry.**

I. Introduction

AIRBORNE radar sounding measurements have been used to characterize the surface, internal structure, and basal properties of glaciers, ice caps, and ice sheets in Antarctica, the Arctic, as well as numerous alpine regions (e.g., the Andes, the Alps, etc.) [1]–[8]. Specific to the glacial bed, radar sounding measurements provide key insight into the organization of subglacial hydrologic systems [9]–[12]. These observations provide critical boundary conditions for the numerical ice-sheet models used to understand and predict current and future glacier dynamics and estimate the cryospheric contribution to possible future sea-level rise in response to a changing climate [13]–[15].

Subglacial drainage patterns present with numerous morphological forms but can be generally differentiated between flat-topped or low-relief water bodies including lakes, sheets, Nye channels, broad channels, canals, and saturated sediments [16]–[20], and topographically positive Röthlisberger (R-) channels that erode into the base of the ice [16], [20]–[23]. Conventional radar sounding has proven well-suited to the detection of the flat-lying subglacial lakes and small water ponding [17], [18], [24]. These features resemble the ideal specular targets that radar sounders are designed to reliably detect. Nye channels have been included in this group as, even though they erode channels with hemispherical cross-sections into the subglacial bed, their radar response is expected to be dominated by the flat water/ice interface. Specialized data processing approaches such as reflectivity, specularity content, and echo abruptness [10]–[12], [24] have all been developed to aid in the identification and interpretation of specular targets. In contrast, topographically positive, half-cylinder R-channels are expected to scatter radio frequency energy diffusively [10], and therefore are more difficult to detect with conventional radar sounding. While cavities also represent a subglacial drainage pattern [20] that may produce diffusive radar reflections, assuming they are uniformly distributed, they will not present with the same degree of anisotropy as continuous R-channels.

Fortunately, subsurface scattering from extended features with circular cross-sections (i.e., cylinders) is a well-studied problem in near-surface ground-penetrating radar (GPR) applications; specifically for environmental and engineering targets such as buried pipes, rebar, and wires [25]. One approach developed for such targets is polarimetric radar, which attempts to fully characterize the backscattering response of a cylinder when illuminated by an electromagnetic (EM) plane wave [25]–[27]. Where smooth, specular targets will backscatter the same amount of energy regardless of the polarization of the incident waveform, cylinders are inherently anisotropic and, as such, the strength of the backscattered signal is dependent on the polarization of the incident radiation [28], [29]. Here, we investigate whether the polarimetric radar concepts originally developed for near-surface GPR applications can be adapted

Manuscript received October 28, 2021; revised January 25, 2022 and March 13, 2022; accepted April 26, 2022. Date of publication May 11, 2022; date of current version June 10, 2022. This work was supported by the G. Unger Vetlesen Foundation and the ESCHER program under NASA Grant 80NSSC20K1134. This is UTIG contribution #3875. *(Corresponding author: Kirk M. Scanlan.)*

Kirk M. Scanlan was with the University of Texas Institute for Geophysics, University of Texas at Austin, Austin, TX 78758 USA. He is now with DTU Space at the Technical University of Denmark, 2800 Kongens Lyngby, Denmark (e-mail: kimis@dtu.dk).

Dillon P. Buhl and Donald D. Blankenship are with the University of Texas Institute for Geophysics, University of Texas at Austin, Austin, TX 78758 USA (e-mail: dillon.buhl@utexas.edu; blank@ig.utexas.edu).

Digital Object Identifier 10.1109/JSTARS.2022.3174473

to the study of active subglacial R-channels. Specifically, this article looks to evaluate the capabilities of a future version of the University of Texas Institute for Geophysics (UTIG) High Capacity Airborne Radar System (HiCARS) [24], [30] modified to transmit and receive backscattered radar signals polarized in two orthogonal directions simultaneously.

The application of polarimetric radar concepts to the study of glaciers and ice sheets is not new [31]–[38]. However, much of this previous work has focused on leveraging polarimetric radar measurements to characterize ice crystal orientation fabric by way of phase anomalies associated with birefringent ice layers [39]. There has so far been little attention paid to polarization dependent backscattering from the glarier bed itself. While some studies include the possibility for anisotropic reflection in their radar propagation models [33], [37], this anisotropy is often framed in terms of changes in specular Fresnel reflection coefficient amplitudes that respond directly to anisotropy in dielectric permittivity. The role of a structurally anisotropic bed and diffusely scattering targets, such as R-channels [10], has yet to be fully investigated from a polarimetric radar perspective.

The rest of this article is organized as follows: Section II introduces the basic conceptual framework of polarimetric radar sounding and presents the closed-form analytical solutions for backscattering from perfect electrically conducting (PEC; infinite conductivity) and perfect dielectric (zero conductivity) cylinders. Section III then presents the modeling approach pursued in order to establish the polarimetric response of infinite half-cylinders with plausible material properties for subglacial R-channels. Section IV expands the modeled results to assess 1) the feasibility of using polarimetric radar sounding to detect and characterize R-channel for an unknown relative orientation of the radar system and the subglacial target and 2) R-channel detectability in practice. Finally, Section V concludes this article.

II. Polarimetric Radar and Analytical Solutions for Infinite Cylinders

Airborne radar sounding involves the transmission of EM waves and the recording of reflected echoes generated as those waves encounter dielectric contrasts at a surface as well as in the subsurface. The expected strengths of surface (P_s) and subsurface ($P_{\rm ss}$) echoes from a generic point target can be expressed through the following radar equations [30], [40]:

$$P_s = \frac{P_t G_t G_r \lambda^2 \sigma_s}{(4\pi)^3 h^4} \tag{1}$$

$$P_{ss} = \frac{P_t G_t G_r \lambda^2 T^2 L_{ice}^2 \sigma_{ss} {g_r}^4}{(4\pi)^3 (h+d)^4 n^2}\ . \tag{2}$$

In both (1) and (2), P_t represents the power of the transmit signal, G_t and G_r represent the transmit and receive antenna gains, respectively, λ is the radar wavelength, and h is the aircraft altitude. Specific to (2), T is the transmissivity of the surface interface, $L_{\rm ice}$ is the one-way dielectric loss in the subsurface, g_r is the nadir refraction gain (a purely geometric term), d is the depth to the subsurface target, and n is the refractive index of the subsurface medium. The remaining terms, σ_s and $\sigma_{\rm ss}$, represent the radar cross-section of the surface and subsurface targets, respectively. It is through these radar cross-section terms that the nature of the dielectric targets (i.e., on the surface and in the subsurface) modify the strengths of the backscattered radar echoes.

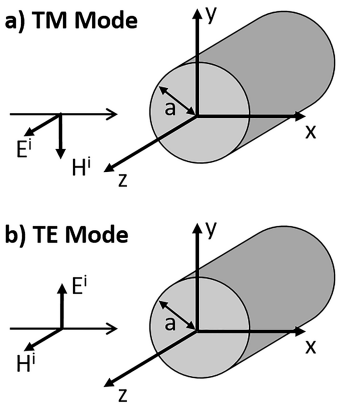

Fig. 1. Illustration of the geometries associated with (a) TM and (b) TE mode electromagnetic plane waves incident on an infinite cylinder of radius a. Adapted from [29].

Conventional radar sounding makes use of antennas that always transmit and record EM waves with a single, linear polarization [24]. Accordingly, the implicit polarization-dependent nature of the radar cross-section terms in (1) and (2) is often overlooked. However, when acquiring radar sounding data in multiple polarizations, any polarimetric variability in the radar cross-sections (σ_s and $\sigma_{\rm ss}$) would help to interpret features on both the surface and in the subsurface. Because the strength of the polarization-dependent echo powers [(1) and (2)] are a function of both the radar cross-sections and instrument parameters (i.e., P_t, G_t, and G_r), here we focus on establishing the radar cross-section of cylindrical and half-cylinder-shaped targets considered to be appropriate representations of subglacial R-channels.

In general, a propagating plane wave can be decomposed into two orthogonal linearly polarized modes (Fig. 1). The cumulative polarization of the plane wave (linear, elliptical, or circular) depends on the amplitude and phase differences between them [25]. In the context of radar backscattering from cylinders, it is common to define an ideal orientation for these two modes where one of the EM field components (either the electric or magnetic field vector) is orthogonal (i.e., transverse) to the long axis of the cylinder (the z-axis in Fig. 1). These two modes are then referred to as the transverse magnetic (TM) and transverse electric (TE) modes, respectively. For this ideal orientation, an infinite cylinder does not behave as a depolarizing scatterer as the polarization of the reflected EM wave is the same as that of the incident wave (i.e., an incident TE mode wave generates only a TE mode reflection).

TM and TE mode scattering from PEC and perfect dielectric infinite cylinders is a well-established problem and there are closed-form analytical solutions for their scattering widths (SWs) [25], [29]. The SW is the two-dimensional (2-D) version

the radar cross-sections (σ_s and $\sigma_{\rm ss}$) introduced in (1) and (2) and is defined as

$$\mathrm{SW} = \lim_{r\to\infty} 2\pi r \frac{|E^s|^2}{|E^i|^2} \tag{3}$$

where $\boldsymbol{r}$ is the distance from the source to the scatterer, E^s is the amplitude of the scattered electric field, and E^i is the amplitude of the incident electric field. The SW quantifies a target's ability to reflect incident EM radiation relative to a perfectly smooth reflector one square meter in size. The TM and TE mode SWs for a PEC cylinder ($\mathrm{SW}_{\mathrm{TM,PEC}}$ and $\mathrm{SW}_{\mathrm{TE,PEC}}$) of radius a are expressed in terms of Hankel and Bessel functions as well as their derivatives (indicated by $'$) [25]

$$\mathrm{SW}_{\mathrm{TM,PEC}} = \frac{2\lambda}{\pi}\left|\sum_{n=0}^{+\infty} \varepsilon_n \frac{J_n(\beta a)}{H_n^{(2)}(\beta a)}\cos(n\phi)\right|^2 \tag{4}$$

$$\mathrm{SW}_{\mathrm{TE,PEC}} = \frac{2\lambda}{\pi}\left|\sum_{n=0}^{+\infty} \varepsilon_n \frac{J_n'(\beta a)}{H_n^{(2)'}(\beta a)}\cos(n\phi)\right|^2. \tag{5}$$

The ε_n term in (4) and (5) is defined to be one when n is zero and two otherwise, while λ is the radar wavelength, β is the radar wavenumber ($2\pi/\lambda$), and ϕ is the scattering angle (defined to be π in the case of backscattering). TM and TE mode SWs for a perfect dielectric cylinder ($\mathrm{SW}_{\mathrm{TM,diel}}$ and $\mathrm{SW}_{\mathrm{TE,diel}}$) of radius a can also be expressed in terms of Hankel and Bessel functions [(6) and (7)], while also requiring relative dielectric permittivity and magnetic permeability ratios ($\varepsilon_{\rm rat}$ and $\mu_{\rm rat}$) between the cylinder and the surrounding materials [25]. Subscripts on the wavenumber terms in (6) and (7), are used to differentiate whether the wavenumber is defined either outside (0) or inside (1) the cylinder.

The analytical solutions to TM and TE mode backscattering from a PEC and perfect dielectric cylinder as a function of cylinder radius are presented in Fig. 2; PEC cylinders in Fig. 2(a) and (b); and dielectric cylinders in Fig. 2(c) and (d). The relative dielectric permittivity of the cylinder and surrounding material used in the calculation of Fig. 2(c) and (d) are 81 and 1; representing a water-filled cylinder suspended in free space [41]. For both cylinder types, analytical solutions are calculated at five frequencies spanning the UTIG HiCARS radar bandwidth (a 15 MHz bandwidth centered at 60 MHZ) [30].

As shown in Fig. 2(a), there is a clear and consistent increase in the TM mode SW of a PEC cylinder with increasing radius, with little variation across the HiCARS bandwidth. While the TE mode SW of a PEC cylinder also generally increases with cylinder radius [Fig. 2(b)], this linear increase is modulated by a frequency-dependent periodicity. As such, for the same PEC cylinder radius, the periodic behavior may yield different TE mode SWs across the radar bandwidth. In contrast to TM and TE mode backscattering from a PEC cylinder, the SW of a perfect dielectric cylinder is much more chaotic. While there is an overarching trend of increasing TM mode SW with increasing cylinder radius [Fig. 2(c)], this increase is overlain by a series of sharp, repeating, and high-amplitude departures (both positive and negative) from that trend. The relative patterns of where these deviations occur as function of both cylinder radius [see their alignment at 2.25 and 4.5 m in Fig. 2(c)] and variation across the HiCARS bandwidth suggest that they are frequency dependent and represent effects of internal constructive and destructive interference occurring within the perfect dielectric cylinder itself. Internal, frequency-dependent interference patterns within a perfect dielectric cylinder are even more pronounced when calculating the TE mode SW [Fig. 2(d)]. The consistent, frequency-independent increase in SW with increasing radius is not as prevalent in the TE mode response as it is for the TM mode, whereas the effects of internal interference are spread over a greater range of cylinder radii [compare the broad interference-related effect at $\sim$4.3 m in Fig. 2(d) with the more radius-restricted patterns in Fig. 2(c)].

Frequency-dependent behavior in SWs of PEC cylinders suggest that it may be possible to detect cylinders and infer their size by comparing TM and TE mode echo powers at different frequencies within the bandwidth. To this end, Fig. 3 presents the difference in TM and TE mode SWs ($\mathrm{SW}_{\mathrm{TM,XX}}$ and $\mathrm{SW}_{\mathrm{TE,XX}}$, where XX refers to the material type; PEC or diel) for the same five HiCARS frequencies as a function of cylinder radius for PEC [Fig. 3(a)] and perfect dielectric cylinders [Fig. 3(b)]. There is clear frequency-dependent periodic behavior in the TM/TE mode difference for a PEC cylinder across the HiCARS bandwidth. Therefore, if it was possible to measure both TM and TE mode backscattering from a PEC cylinder using HiCARS, it may be possible to leverage the difference in TE mode and TM mode echo powers to not only detect PEC cylinders (through a polarization-dependent change in reflected echo power) but estimate their size as well (by comparing that change across the signal bandwidth).

The same cannot be said for TM and TE mode backscattering from a perfect dielectric cylinder [Fig. 3(b)]. Unlike for the PEC cylinder, the TM/TE mode differences exhibit no consistent systematic behavior across both the HiCARS bandwidth and cylinder radii that could be used to infer cylinder size. Note, however, that large, isolated deviations from the general TM/TE difference behavior do tend to become more prevalent for larger cylinder radii. If a substantial increase or decrease in the TM/TE mode difference were to be observed for a specific frequency

$$\mathrm{SW}_{\mathrm{TM,diel}} = \frac{4}{\beta_0}\left|\sum_{n=-\infty}^{+\infty} \frac{J_n'(\beta_0 a)\,J_n(\beta_1 a) - \sqrt{\varepsilon_{\rm rat}/\mu_{\rm rat}}\,J_n(\beta_0 a)\,J_n'(\beta_1 a)}{\sqrt{\varepsilon_{\rm rat}/\mu_{\rm rat}}\,J_n'(\beta_1 a)\,H_n^{(2)}(\beta_0 a) - J_n(\beta_1 a)\,H_n^{(2)'}(\beta_0 a)} e^{jn\phi}\right|^2 \tag{6}$$

$$\mathrm{SW}_{\mathrm{TE,diel}} = \frac{4}{\beta_0}\left|\sum_{n=-\infty}^{+\infty} \frac{J_n'(\beta_0 a)\,J_n(\beta_1 a) - \sqrt{\mu_{\rm rat}/\varepsilon_{\rm rat}}\,J_n(\beta_0 a)\,J_n'(\beta_1 a)}{\sqrt{\mu_{\rm rat}/\varepsilon_{\rm rat}}\,J_n'(\beta_1 a)\,H_n^{(2)}(\beta_0 a) - J_n(\beta_1 a)\,H_n^{(2)'}(\beta_0 a)} e^{jn\phi}\right|^2 \tag{7}$$

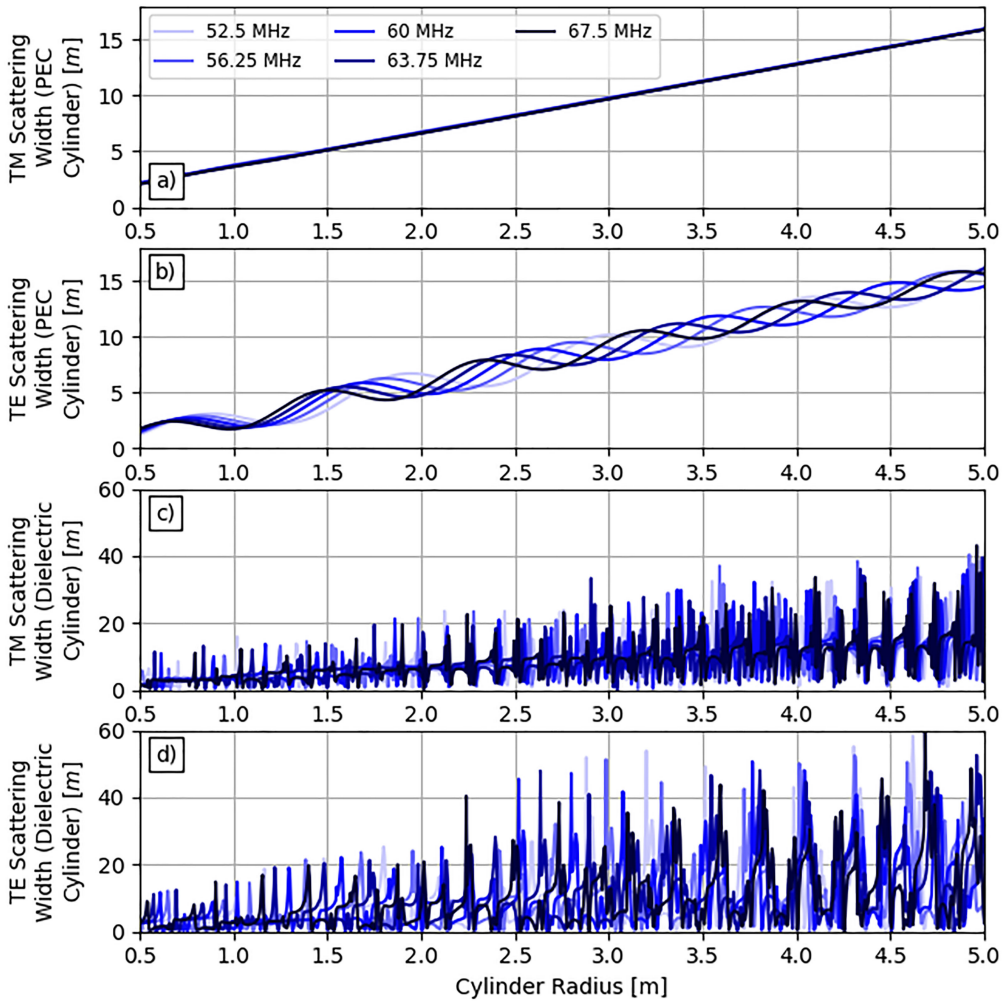

Fig. 2. Analytical TM mode [(a) and (c)] and TE mode [(b) and (d)] scattering widths for PEC [(a) and (b), infinite conductivity] and perfect dielectric [(c) and (d), conductivity of zero and relative dielectric permittivity of 81] infinite cylinders as a function of cylinder radius for five frequencies spanning the HiCARS bandwidth (52.5 to 67.5 MHz). The PEC cylinder scattering widths are both smoother and more systematic compared to those for the dielectric cylinders. A 0.5 cm increment is used to vary the radius of the PEC and dielectric cylinders between 0.5 and 5.0 m.

relative to the others within the bandwidth, it may be possible to then generalize that the cylinder exhibits a large (>2 m) radius.

III. Methods-of-Moments Modeling of Infinitely Long Half-Cylinders

While (4) through (7) provide important insight for near surface GPR studies [25] and are useful for introducing polarimetric radar concepts, they are less useful when investigating radar scattering from subglacial R-channels. This is for two reasons. First, subglacial R-channels are not perfect cylinders (i.e., they do not exhibit a full circular cross-section [10]). Second, subglacial R-channels are neither perfect electrical conductors (infinite conductivity) nor perfect dielectrics (zero conductivity) but voids at the base of the ice that are assumed to be filled with water. It is therefore difficult to infer R-channel TM and TE mode backscattering behavior based on Figs. 2 and 3 and an alternative approach is required.

The approach adopted in this analysis is method-of-moments (MOM) modeling using the Altair Feko$^{\mathrm{TM}}$ software package [42]. MOM simulations within Altair Feko$^{\mathrm{TM}}$ are highly adaptable to varying scatterer geometries including the small, curved surfaces required for R-channels. These types of surfaces are difficult to represent with other closed-form solutions for radar backscattering, such as decomposing the R-channel into individual facets. In order to capture the small-scale geometries, individual facets would have to be less than a wavelength in size. Curved surfaces are also difficult to reproduce using standard finite-difference time-domain modeling software such as gprMax [43], as domain decomposition is performed using 3-D rectangular Yee cells. All MOM simulations are performed using two orthogonal sources, one for each of the TM and TE mode polarizations (Fig. 1). Each source transmits a monochromatic, linearly polarized, unit amplitude, and plane wave, and is placed 500 wavelengths (∼2.5 km) from the target. The intervening material between the source and the target is free space.

The first set of simulations looks to reproduce the analytical TM and TE mode SWs for infinite PEC and perfect dielectric

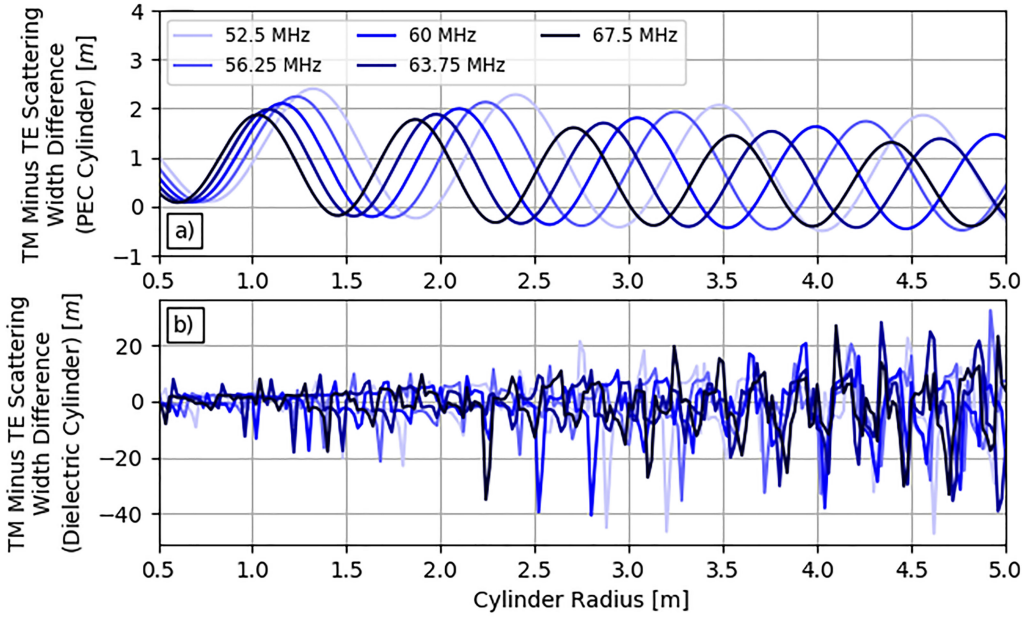

Fig. 3. Difference between analytic TM mode and TE mode scattering widths as a function of (a) PEC and (b) dielectric infinite cylinder radius. Resonances in the PEC response (a) suggest it may be possible to infer cylinder size by comparing the scattering width difference for different frequencies. While the dielectric scattering width difference amplitudes (b) are large, there is no clear, overarching systematic behavior that could be leveraged to infer cylinder radius.

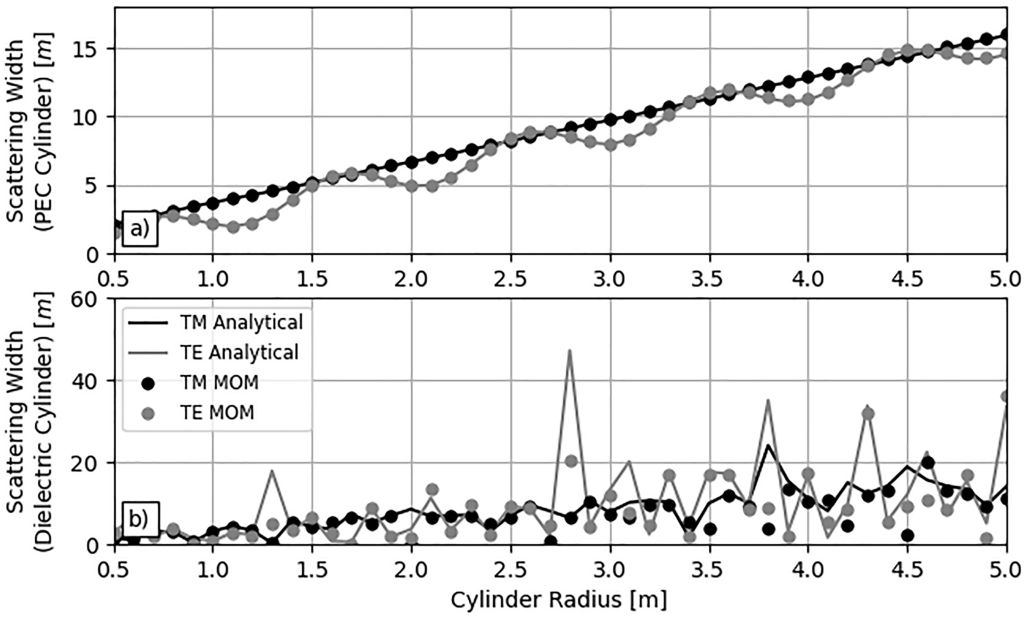

Fig. 4. Comparison of analytical and MOM (a) PEC and (b) dielectric scattering widths for infinite cylinders. The general agreement between the results provides confidence that method-of-moments (MOM) simulations can be used to evaluate polarimetric backscattering from half-cylinder, water-filled channels. Note that because analytical and MOM scattering widths are calculated at intervals of 0.1 m, the internal interference effects observed in the scattering width of a perfect dielectric cylinder [Figs. 2(c) and (d)] are not always captured.

(ε_r of 81) cylinders to ensure the MOM approach is behaving as expected. The PEC cylinder results for both the TM and TE modes are presented in Fig. 4(a), while the perfect dielectric cylinder results are presented in Fig. 4(b). The cylinder radius is varied from 0.9 to 3.1 m in 0.1 m increments for both the MOM simulations and analytical solutions, and the frequency of the incident plane wave is 60 MHz. Fig. 4(a) reveals that the MOM simulations perfectly replicate the analytical TM and TE mode SWs for a PEC cylinder. However, for the dielectric cylinder [Fig. 4(b)], the agreement between the analytical and MOM simulation results is not as uniform. Both the TM and TE mode MOM simulations exhibit some difficulty in reproducing the analytical results in some areas where small changes in cylinder radius result in large changes in SW (e.g., the TM mode at 3.8

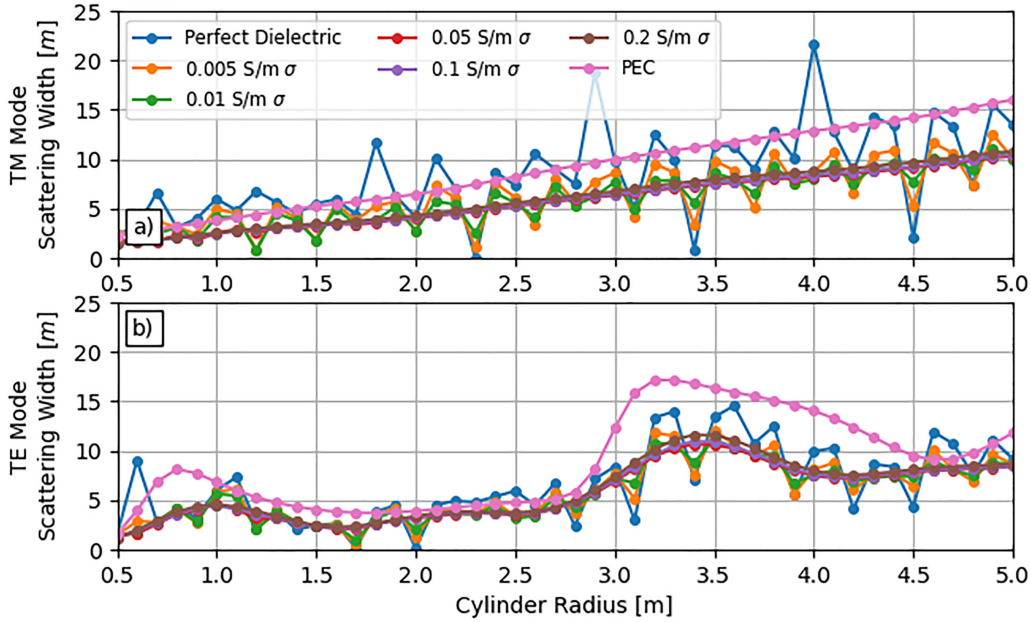

Fig. 5. MOM simulation results for the (a) TM mode and (b) TE mode scattering widths of half-cylinders as a function of cylinder radius and cylinder conductivity. All MOM simulations are performed using a monochromatic 60 MHz plane wave. Once the conductivity of the cylinder exceeds 0.05 S/m, the scattering width response for both modes behaves as a muted version of the systematic PEC response.

and 4.5 m and the TE mode at 1.3, 2.8, and 3.8 m). Except for these local deviations, there is a good agreement between the analytical TM and TE mode SWs and those produced by the MOM simulations. As the MOM simulation results generally agree with the analytical solutions, there is a confidence that MOM simulations can be used to investigate radar backscattering from R-channels.

Nadir water-filled R-channels within the MOM simulations are represented as infinite dielectric half-cylinders (i.e., cylinders in Fig. 1 cut along the *yz*-plane [10]) suspended in free space with a relative dielectric permittivity of 81 [41] and an initially variable conductivity. While subglacial R-channels are neither infinitely long nor floating in free space, these simplifications to the MOM models will not affect this analysis of polarimetric R-channel SWs for numerous reasons. First, we consider subglacial R-channels that are straight within the pulse-limited footprint of the radar (i.e., are effectively infinite from the perspective of the radar). For context, the radius of the HiCARS (15-MHz bandwidth) pulse-limited (i.e., nonsynthetic aperture radar (SAR) focused) footprint under 2000 m of ice [10] (ε_r of 3.15) from an altitude of 500 m (nominal HiCARS height above surface) is approximately 180 m. Second, for flat interfaces and normal incidence angles, the TM and TE Fresnel reflection and transmission coefficients are the same [28], [29]. Therefore, since it is assumed that the air–ice interface [incorporated as a transmissivity in (2)] as well as the glacier bed surrounding the R-channel within the pulse limited footprint are flat, they will not contribute any polarization-dependent effects. Even for rough surfaces (such as those within the validity range of the small perturbation model), the copolarized (*hh* and *vv*) scattering coefficients at normal incidence are the same [44], [45]. Third, we assume that the beam patterns associated with the orthogonal antennas generating the TM and TE plane waves and recording the reflected response are equivalent [G_t is equal to G_r in (2)]. Finally, we ignore the effects of anisotropic crystal fabric [31]–[38] and assume radar propagation and attenuation [L_{ice} in (2)] within the ice column is not polarization dependent. Taken together, the only polarization-dependent term in (2) that would differentiate the received echo powers between the two modes is the radar cross-section (or its 2-D equivalent SW). Note that as this article intends to build on the radar observations of discrete R-channels reported in [10], the implications of R-channel networks (i.e., multiple, closely spaced R-channels of potentially variable sizes) or partially water-filled R-channels are considered beyond the current scope.

The SW of a half-cylinder at 60 MHz as a function of radius and conductivity are presented in Fig. 5 [TM mode in Fig. 5(a) and the TE mode in Fig. 5(b)]. The radius of the half-cylinder is varied in 0.1 m increments between 0.5 and 5.0 m (taken as a representative range for likely R-channel radii [23]), while cylinder conductivity is varied between 0.005 and 0.2 S/m. The SWs of perfect dielectric and PEC half-cylinders at these radii are also presented. For context, the conductivity of freshwater is known to vary between 0.0001 and 0.01 S/m, while the conductivity of sea water is 4 S/m [41]. Furthermore, airborne transient EM measurements in Antarctica have revealed water conductivities between approximately 0.01 and 5 S/m for subglacial fresh water and brines, respectively [46].

The MOM simulations reveal a consistent pattern to both the TM and TE mode responses as the conductivity of the half-cylinder is varied. For perfect dielectric and PEC simulations, the results are similar to what has been observed for the analytical solutions (Fig. 2). The PEC responses are well defined, while the perfect dielectric responses follow a general trend but are overlain by highly variable departures from that trend related to internal reflection effects. It is worthwhile to note, however, that

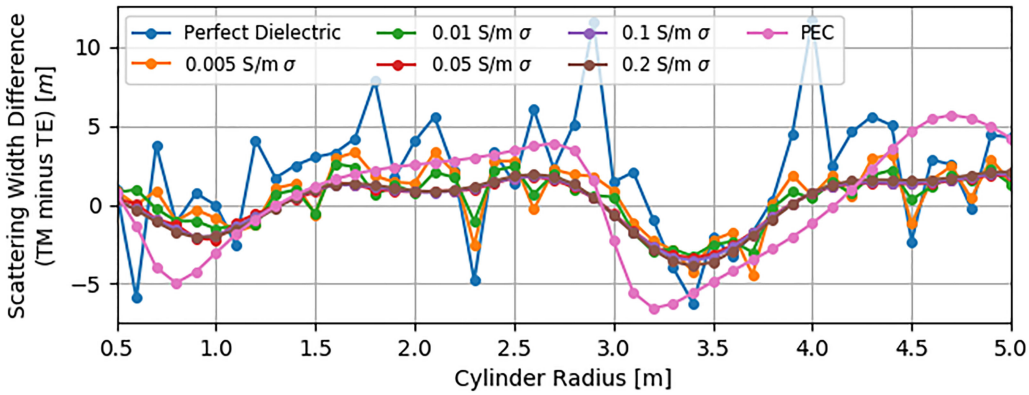

Fig. 6. Difference between the MOM simulated TM mode and TE mode scattering widths of half-cylinders as a function of cylinder radius and cylinder conductivity. Once the conductivity of the cylinder exceeds 0.05 S/m, the scattering width response for both modes behaves as a muted version of the PEC difference.

the amplitudes of these deviations for a half-cylinder are not as large as those for a full cylinder [i.e., compare Fig. 5(a) with Fig. 2(c)]. As the conductivity of the dielectric half-cylinder is increased, the highly fluctuating behavior in the TM and TE responses decreases, eventually yielding a much more systematic response for a conductivity of 0.05 S/m. This is expected as an increasing half-cylinder conductivity implies greater radar wave attenuation within the half-cylinder, thereby reducing the impact of internal reflections. At even greater conductivities, there is only minor change in the TM and TE SWs. The TM and TE mode responses above 0.05 S/m resemble muted versions of the PEC response, in that they have similarly shaped variability with respect to cylinder radius but reduced amplitudes.

The collapse of the individual TM and TE mode SW responses to a smoother behavior at conductivities above 0.05 S/m also results in a smoother response of the difference between the two modes (Fig. 6). As observed for the TM and TE modes individually (Fig. 5), the TM/TE mode difference behaves as a muted version of the PEC response. The smaller absolute differences between the TM mode and TE mode SWs compared to the PEC scenario imply that for any field implementation of polarimetric radar sounding, stringent controls will be required on the radiometric stability and radiometric resolution of the acquisition system. If the acquisition system design is not robust enough to detect small changes in reflected echo powers associated with small variations in the TM and TE mode SWs, it will not be possible to infer the existence of subglacial R-channels exhibiting specific radii.

Following Figs. 2 and 3, Fig. 7 presents half-cylinder MOM simulation results (TM and TE mode SWs as well as their difference) at five frequencies spanning the HiCARS bandwidth. A cylinder conductivity of 0.05 S/m is used in all simulations presented in Fig. 7. Following the analytical PEC results, the TM and TE mode responses across the bandwidth [Fig. 7(a) and (b)] have a similar pattern but are horizontally offset from one another as a function of frequency. As such, the TM/TE mode difference [Fig. 7(c)] is also offset. Unlike the analytical PEC results [Fig. 3(a)], there is no consistent periodic behavior in the TM/TE mode difference across all cylinder radii. This is because the TE mode response of a water-filled half-cylinder [Fig. 7(b)] does not exhibit the same periodic behavior as a circular PEC cylinder [Fig. 2(b)]. Fig. 7(c) implies that it may be difficult to estimate R-channel size from the TM/TE mode SW difference across the HiCARS bandwidth for some cylinder geometries. The most obvious example is for R-channels with radii between 1.5 and 2.5 m where there is minimal separation between the TM/TE mode differences as a function of frequency. However, below 1.5 m and above 2.5 m, the differences in the TM mode TE mode SWs across the HiCARS bandwidth increase. This suggests that the radius of subglacial R-channels could be inferred by comparing the differences in reflected echo powers across different signal frequency subbands.

IV. Feasibility of Field Implementation

A. Relative Orientation of Antennas and R-Channels

The TM and TE mode SWs derived from MOM simulations presented in the previous section imply that it may be possible to detect and characterize the radius of subglacial R-channels with polarimetric radar sounding by comparing TM and TE mode echo powers. However, all MOM simulations discussed so far consider an ideal orientation of the antennas such that the TM and TE modes are measured (i.e., one EM field vector is always aligned with the long axis of the cylinder, Fig. 1). Any attempt to implement polarimetric radar sounding in practice will not be able to guarantee that this assumption is universally met. Therefore, in order to represent a feasible approach for R-channel detection and delineation, the effects of an unknown relative orientation of the antennas and the R-channel must be considered.

The backscattered response of a target when illuminated with an arbitrarily polarized plane wave is described using a 2-D scattering matrix (S) [25]

$$S = \begin{bmatrix} S_{AA} & S_{AB} \\ S_{BA} & S_{BB} \end{bmatrix}. \tag{8}$$

The elements of the scattering matrix are the measured reflection amplitudes, while the A and B subscripts refer to two arbitrary yet orthogonal antenna polarization directions. The order of the subscripts refers to which antenna serves as the

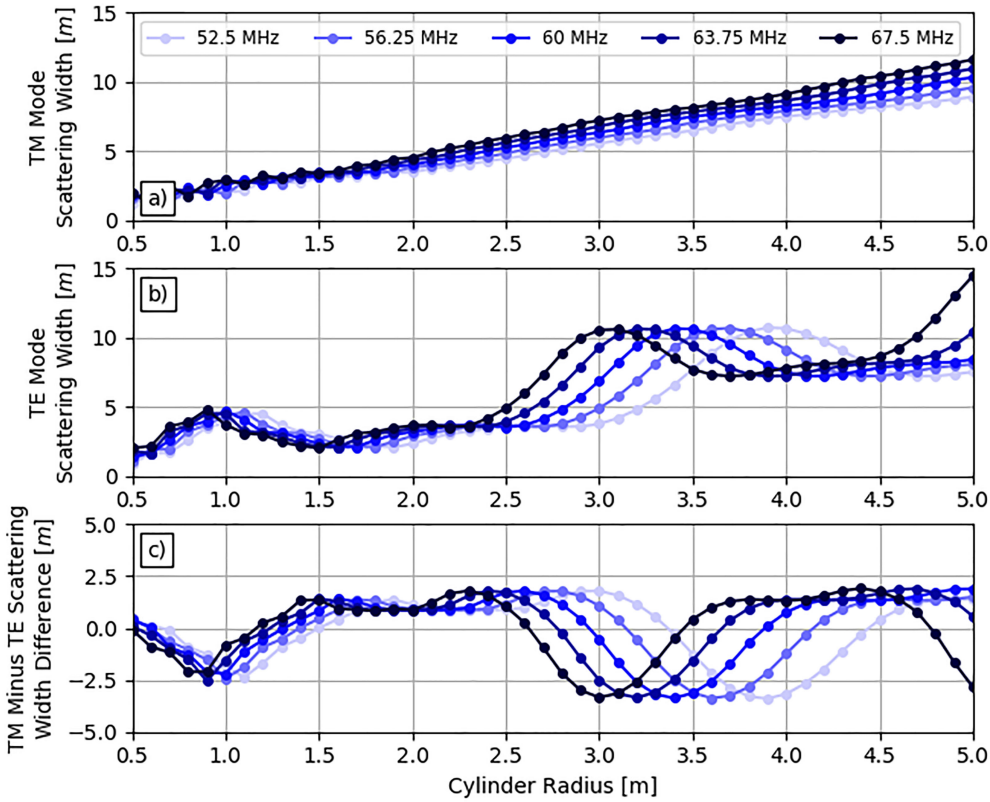

Fig. 7. MOM simulation results for the (a) TM mode scattering width, (b) TE mode scattering width, and (c) TM/TE mode scattering width difference of a half-cylinder as a function of cylinder radius and incident radar wave frequency. All MOM simulations use a cylinder conductivity of 0.05 S/m. Separation between TM mode and TE mode scattering widths is only observed for radii greater than 2.5 m.

receiver (first subscript) and the transmitter (second subscript). For example, the S_{AB} term refers the backscattered amplitude measured with the *A*-directed antenna after initially illuminating the target with a *B*-directed linearly polarized wave. In the context of the geometry presented in Fig. 1, if the *A*-directed antenna is defined as being aligned with the strike of the cylinder (the *z*-direction), the S_{AA} component is equivalent to the TM mode, while the S_{BB} component represents the TE mode. In order to fully populate the scattering matrix, it is necessary for the acquisition system to be capable of both transmitting and receiving linearly polarized radar waves in the *A* and *B* directions independently. That is, the acquisition system must have the capacity to transmit from the *A*-directed antenna while recording using both *A* and *B* antennas (populating S_{AA} and S_{BA}) before switching and transmitting from the *B*-directed antenna (populating S_{AB} and S_{BB}).

Additional MOM simulations are used to investigate the variability in the individual scattering matrix elements for any arbitrary antenna polarization and R-channel radius. In lieu of populating the scattering matrix with actual backscattered amplitudes, the individual elements are populated with the associated SWs, as they are assumed to be the only polarization-dependent terms in the radar equation (2). Fig. 8 presents the SWs derived from the amplitude of each element in the scattering matrix for 0.5, 1.0, 1.5, and 2.0 m radii R-channels as a function of antenna orientation. An R-channel conductivity of 0.05 S/m and a source wave frequency of 60 MHz are used in all MOM simulations presented in Fig. 8. The polarization angle is the angle between the *A*-directed antenna and the long axis of the R-channel and is varied between 0° and 180° in 5° increments.

As expected, for polarization angles of 0° and 180°, the S_{AA} [Fig. 8(a)] and S_{BB} [Fig. 8(b)] SWs are equivalent to those that would be measured in the ideal TM and TE mode orientation (Fig. 5). When rotated by 90°, the situation is reversed with S_{AA} corresponding to the ideal orientation for measuring the TE mode response, while S_{BB} yields the ideal TM mode response. In either scenario, when one of the antennas is aligned with the long axis of the R-channel, the cross-polarized components of the scattering matrix (S_{AB} and S_{BA}) are zero.

For all other polarization angles in Fig. 8(a) and (b), the like-polarized components of the scattering matrix deviate from the ideal TM and TE mode responses. The nature of that deviation is a function of the R-channel radius. In terms of the off-diagonal components [Fig. 8(c)], for an individual R-channel radius, the SWs are equivalent ($S_{AB} = S_{BA}$) and they attain a maximum value at polarization angles of 45° and 135° (45° + 90°). The 0.5-m radius R-channel exhibits a significant cross-polarized response that, when maximized, approaches the strength of the like-polarized components (S_{AA} and S_{BB}). However, energy in the cross-polarized elements quickly degrades for all polarization angles as the R-channel radius is increased. In this way, large radius R-channels behave similarly to infinite circular cylinders in that they do not scatter depolarized energy when illuminated with plane waves [25].

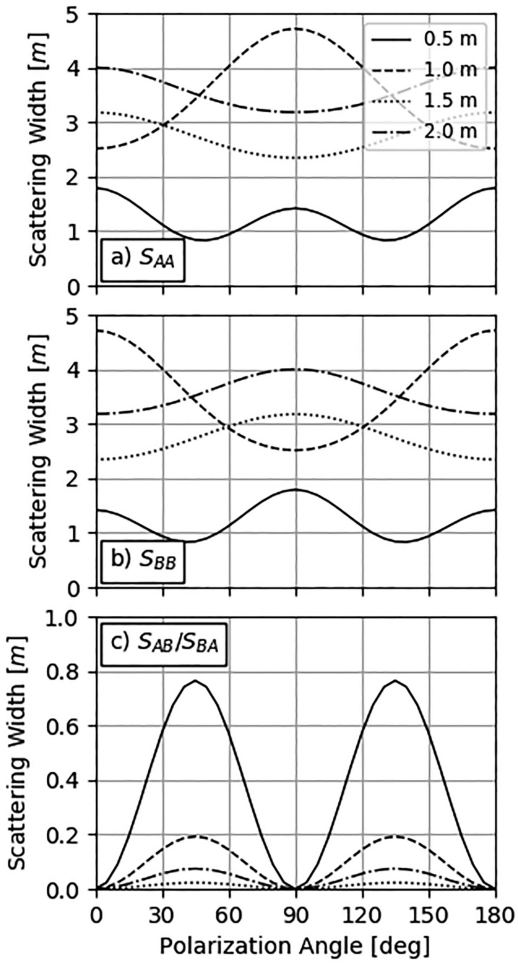

Fig. 8. Polarimetric response for four infinitely long half-cylinders (radii of 0.5, 1.0, 1.5, and 2.0 m) as a function of polarization angle at 60 MHz. The polarization angle is the angle between an *A*-directed antenna and the infinite axis of the half-cylinder [see Fig. 1(a)]. For radii greater or equal to 1 m, the S_{AA} and S_{BB} components [(a) and (b)] of the scattering matrix are either maximized or minimized (depending on cylinder radius) at intervals of 90° starting from 0°. The like-polarized scattering matrix components (S_{AA} and S_{BB}) are equal at 90° increments of 45°. As demonstrated in (c), except for very small half-cylinders (0.5-m radius), subglacial R-channels are not expected to be strong depolarizers (S_{AB} and S_{BA} are small).

Turning to the polarization angle dependency in the like-polarized components [Fig. 8(a) and (b)], the 0.5 m radius R-channel exhibits a distinctly different behavior compared to the others (1.0, 1.5, and 2.0 m). For these larger R-channels, the S_{AA} and S_{BB} SWs exhibit a smooth transition between the ideal TM and TE mode endmembers (compare the 0° polarization S_{AA} and S_{BB} SWs with TM and TE mode values in Fig. 5). All SW amplitudes at intermediate polarization angles are somewhere between those of the ideal TM and TE modes. In contrast, for an R-channel radius of 0.5 m, the ideal TM and TE mode SW amplitudes represent local maxima with consistently smaller SWs at intermediate polarization angles. This behavior is a result of the more substantial depolarization effects [S_{AB} and S_{BA}; Fig. 8(c)] associated with small radii R-channels.

The polarization angle dependence of the like-polarized SWs exemplified in Fig. 8(a) and (b) introduces significant complications when attempting to use the TM/TE mode (S_{AA}/S_{BB}) difference to both detect subglacial R-channels and estimate their size. This is because the difference in like-polarized SWs is maximal when one antenna polarization is parallel to the long axis of the R-channel (i.e., 0°, 90°, and 180°), while less for all other intervening polarization angles. The most extreme situation is for polarization angles of 45° and 135°, where the like-polarized SWs are equivalent, and as such, an R-channel of any size cannot be discriminated from a generic interface generating an equally strong polarization-independent reflection. Even though the cross-polarized SWs are maximized at 45° and 135°, associated reflections are unlikely to be strong enough such that they exceed the radar noise floor.

Taken together, the feasibility of implementing polarimetric airborne radar sounding for the detection and characterization of subglacial R-channels will depend on the radiometric precision of the acquisition system (i.e., how well a reflected power can be measured for an individual channel) as well as the radiometric stability between the different like-polarized receive channels (S_{AA} and S_{BB}). To this end, Fig. 9 presents the S_{AA}/S_{BB} SW difference envelope as a function of both R-channel radius and polarization angle. Similar to Fig. 8, as the polarization angle approaches 45°, the difference in received power between the like-polarized components decreases and will become more difficult to detect. Based on Fig. 7, the scattering envelopes for other frequencies within the HiCARS bandwidth can be expected to be slightly shifted version of the 60 MHz envelope shown in Fig. 9. As an example, even though the 60 MHz S_{AA}/S_{BB} SW difference is zero for a half-cylinder radius of 3.9 m (Fig. 9), the difference at other frequencies within the HiCARS bandwidth will be nonzero (Fig. 7). By combining the results of Figs. 7 and 9 into (2), along with the instrument-defined parameters such as transmit power and antenna gains, it would be possible to assess how well an acquisition system operating over the HiCARS bandwidth can detect subglacial R-channels. There will ultimately be an instrument specific, minimum resolvable difference between S_{AA} and S_{BB} echo powers that will define the radii of R-channels that can be detected and whose cross-bandwidth response can be leveraged to infer R-channel size [Fig. 7(c)]. This same minimum resolvable difference will also define an acceptable level of relative misalignment between the orientation of the acquisition system and the strike of any detectable R-channel (Fig. 9).

B. Considerations for Geologic Setting

Provided a future polarimetric airborne radar sounding system meets a requisite radiometric precision and cross-channel stability, variations in modeled SWs suggest that it may be possible to both detect subglacial R-channels (a polarization-dependent difference in backscattered power) and infer their size (frequency-dependent behavior of that power difference across the bandwidth). However, the MOM simulations say nothing about the ability to detect reflections from R-channels through an overlying ice column. R-channels exist as discrete features at the glacial bed and are therefore subject to higher geometric spreading losses compared to a flat interface [30], [40] while also being subject to englacial attenuation [47]–[49]. An assessment

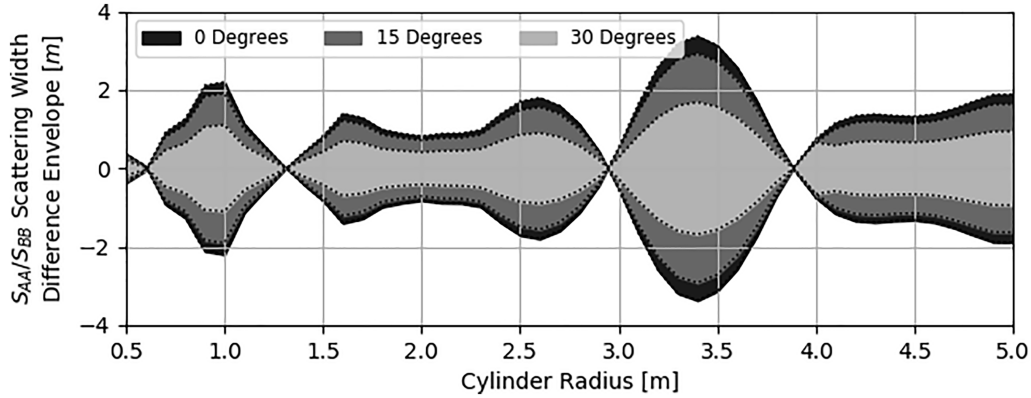

Fig. 9. S_{AA} and S_{BB} scattering width difference envelope as a function of cylinder radius and polarization angle at 60 MHz. Note that at 45°, the S_{AA} and S_{BB} scattering widths are equivalent and the difference is always zero.

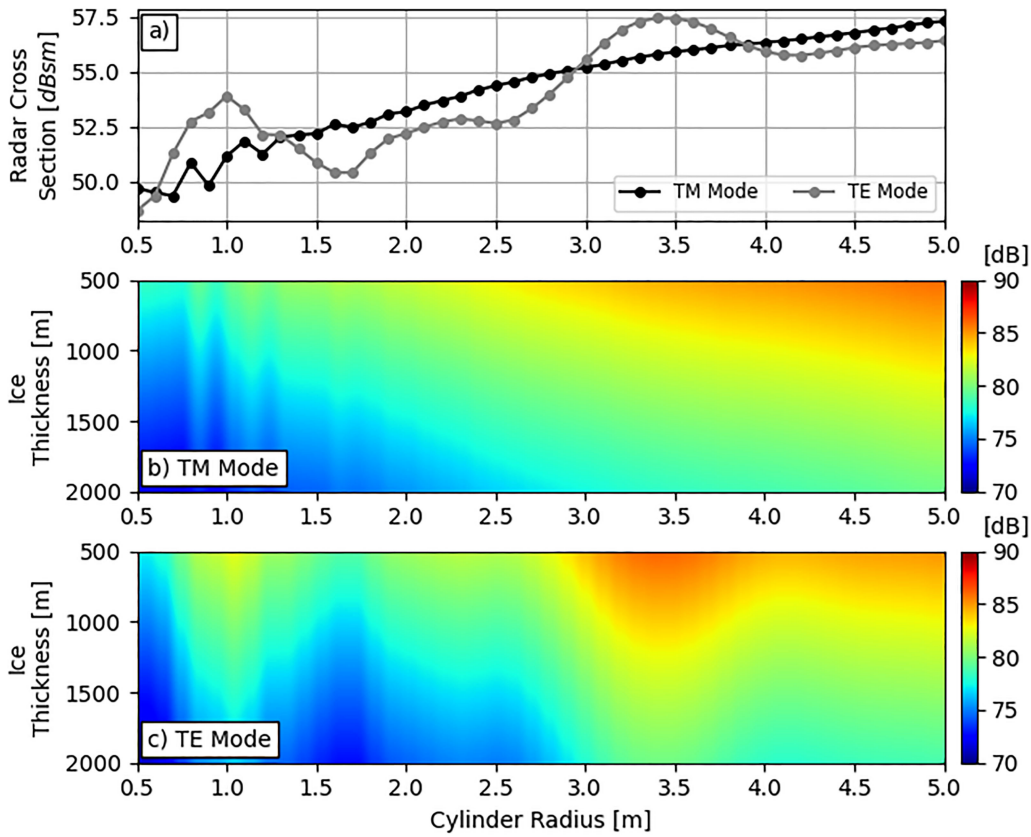

Fig. 10. Assessment of R-channel detection feasibility. (a) TM and TE mode radar cross-sections at 60 MHz for a half cylinder R-channel (0° polarization angle, ε_r of 81, and conductivity of 0.05 S/m) under 2000 m of ice. (b) TM mode excess signal strength as a function of R-channel radius and ice thickness. (c) TE mode excess signal strength as a function of R-channel radius and ice thickness. Larger excess signal strength implies larger englacial attenuation rates can be tolerated before the reflection from the subglacial R-channel becomes too weak to be measured. Minimum detectable signal is defined as −125 dBm.

of the feasibility that TM and TE mode reflections from an individual R-channel could be detected by a future polarimetric radar sounding system with a similar footprint to HiCARS [24] but with a 60 MHz monochromatic signal is presented in Fig. 10.

First, Fig. 10(a) presents the results of translating TM and TE mode SWs (0° polarization angle, ε_r of 81, and conductivity of 0.05 S/m) to radar cross-sections following the method outlined in [29]

$$\text{RCS} \simeq \text{SW} * \frac{2l^2}{\lambda}. \tag{9}$$

In order to convert the 2-D SW to a 3-D radar cross-section, the length of the half-cylinder [l in (9)] must be specified. As this article assumes straight subglacial R-channels located at nadir,

this length is equivalent to the diameter of the pulse-limited footprint (assuming the full 15 MHz HiCARS bandwidth) for a particular ice thickness. A 2000-m-thick ice column is used in the generation of Fig. 10(a) thereby implying an R-channel length of 360 m. Note that while SAR processing would decrease the size of the effective radar footprint [50]–[52], it is not considered as part of this article as only the radar response of the R-channels at nadir is modeled.

Once the radar cross-section of an R-channel can be defined as a function of overlying ice thickness (d), that value can be used in (2) to predict absolute received echo strength. This prediction though requires *a priori* knowledge of acquisition system parameters such as transmit power (P_t), transmit (G_t), and receive (G_r) antenna gains as well as englacial attenuation (L_{ice}). As an illustrative example, this article adopts HiCARS values for the transmit power (67 dBm) and total antenna gain (9 dB) [24]. Since englacial attenuation rates vary by location (i.e., [49]), in lieu of deriving absolute expected subglacial R-channel echo powers, this article calculates the difference between the attenuation-neglected reflection strengths and the minimum detectable signal limit for HiCARS (-125 dBm [24]). Excess reflection strengths (values greater than 0 dB) then represent the amount of signal strength that can be lost to attenuation before the R-channel reflection would be too weak to be detected. The excess reflection strength results for the TM and TE modes as a function of ice thickness and R-channel radius are presented in Fig. 10(b) and (c) , respectively. Note however, that as these results are based on HiCARS parameters, a different acquisition system with a different set of parameters (i.e., transmit power, antenna gain, and minimum detectable signal) would produce a different result.

Nonetheless, the results in Fig. 10(b) and (c) can be used to provide general insight into where TM and TE mode reflections from subglacial R-channels can be expected to be observed. For example, consider the variation in observed attenuation rates across Greenland [49]. In the interior, where attenuation rates are lowest ($\sim$5 dB/km), even the smallest considered R-channels (0.5 m radius) would be easily detectable under 2 km of ice ($\sim$20 dB two-way attenuation losses against $\sim$70 dB of excess signal strength). As attenuation rates increase toward the margin (approaching 25 dB/km), it becomes progressively more challenging to detect small R-channels even though the overlying ice thickness decreases. The substantial excess signal strengths for large R-channels imply that, for a polarimetric acquisition system with similar performance capabilities to HiCARS and based on measured attenuation rates [49], these features would be detectable under the Greenland Ice Sheet.

The results in Fig. 10(b) and (c) can also be used to provide insight on the detectability of a subglacial R-channel relative to the surrounding subglacial bed. Bed echo powers can be predicted following a similar approach to what has been done for the subglacial R-channels but using an alternate version of the radar equation for nonpoint targets [30], [40]. Predictions of bed echo powers will require knowledge of expected local subglacial conditions (i.e., topography, small-scale roughness, and dielectric contrast). Excess signal strength values for the both an R-channel of a specific size and the background bed echo can then be compared in order to assess their relative strength. Previous radar sounding measurements [10] have demonstrated that reflections from subglacial R-channels do dominate relative to reflections from the surrounding subglacial bed under more than 2 km of ice at Thwaites, Antarctica.

Finally, whether frequency-dependent attenuation [47]–[49] would have to be considered when comparing the TM/TE mode difference across the bandwidth in order to infer R-channel size (Fig. 7) depends on the radiometric resolution with which the individual TM and TE components can be measured. Previously observed rates of frequency-dependency in attenuation (i.e., $\sim$8 dB between 110 and 500 MHz [47]) imply that attenuation rate variability across the HiCARS bandwidth is likely be small ($<$0.5 dB). If the radiometric resolution of a future HiCARS-based polarimetric system is fine enough such that sub-dB changes in reflected power can be reliably resolved, frequency-dependent attenuation rates would have to be considered. They would have to be corrected for such that the measured cross-bandwidth TM/TE mode difference to accurately represent scattering from the R-channel. Future polarimetric radar sounding systems that may incorporate a wider bandwidth would be subject to larger, frequency-dependent changes in attenuation rate. These changes would have to be accounted for even if the radiometric resolution of the system was coarse. Of course, the required radiometric resolution in these future systems would also be driven by expected changes in TM and TE mode scattering across the wider bandwidth.

V. Conclusion

The organization of subglacial drainage patterns is a critical factor in the prediction of future glacial flow dynamics. However, while conventional airborne radar sounding strategies are well-suited to the detection of flat-lying water bodies, they are currently limited in their ability to detect topographically positive, diffusively scattering R-channels. This article presents an analysis of how polarimetric radar sounding measurements might be leveraged to study these unique subglacial features.

MOM simulations across the HiCARS bandwidth reveal polarization- and frequency-dependent changes in the radar scattering from half-cylinders exhibiting relative dielectric permittivities and electrical conductivities feasible for a subglacial R-channel. These suggest that both R-channel existence and size may be extractable from a careful analysis of future airborne polarimetric radar measurements. However, the relative orientation of the R-channel to a pair of orthogonal radar antennas is a critical factor. The maximum polarimetric response is observed only when one of the antennas is aligned parallel to the strike of the R-channel (with the other antenna being orthogonal) and quickly degrades for all other alignments. Finally, when placed in the context of radar sounding through an ice column, local and possibly frequency-dependent attenuation rates exert significant influence on the ability to detect these small subglacial features.

This article provides a critical assessment of radar scattering from subglacial R-channels and the factors that must be considered during the design of a polarimetric radar system to study them. It highlights that the feasibility of using polarimetric

radar sounding to study subglacial R-channels is intimately tied to the radiometric precision and cross-channel stability inherent in the acquisition system. The results highlight that the ability to consistently resolve dB and ideally sub-dB scale differences between the different polarization echo strengths is critical in order to characterize subglacial R-channels. Existing and future instruments will have to define their performance in these fields in order to assess the types of R-channels they may be capable of studying.

Acknowledgment

The authors would like to thank C. Gerekos and D. A. Young for their insightful comments and critiques during the preparation of this article. The authors would also like to thank three anonymous reviewers whose comments materially improved the quality of this article.

References

[1] J. A. Dowdeswell and S. Evans, "Investigations of the form and flow of ice sheets and glaciers using radio-echo sounding," *Rep. Prog. Phys.*, vol. 67, no. 10, pp. 1821–1861, Oct. 2004, doi: 10.1088/0034-4885/67/10/R03.

[2] R. G. Bingham and M. J. Siegert, "Radio-echo sounding over polar ice masses," *J. Environ. Eng. Geophys.*, vol. 12, no. 1, pp. 47–62, Mar. 2007, doi: 10.2113/JEEG12.1.47.

[3] N. B. Karlsson, D. M. Rippin, R. G. Bingham, and D. G. Vaughan, "A 'continuity-index' for assessing ice-sheet dynamics from radar-sounded internal layers," *Earth Planet. Sci. Lett.*, vol. 335–336, pp. 88–94, Jun. 2012, doi: 10.1016/j.epsl.2012.04.034.

[4] A. Rutishauser, H. Maurer, and A. Bauder, "Helicopter-borne ground-penetrating radar investigations on temperate alpine glaciers: A comparison of different systems and their abilities for bedrock mapping," *Geophysics*, vol. 81, no. 1, pp. WA119–WA129, Jan. 2016, doi: 10.1190/GEO2015-0144.1.

[5] A. Rutishauser *et al.*, "Characterizing near-surface firn using the scattered signal component of the glacier surface return from airborne radio-echo sounding," *Geophys. Res. Lett.*, vol. 43, no. 24, pp. 12502–12510, Dec. 2016, doi: 10.1002/2016GL071230.

[6] G. Gacitúa, J. A. Uribe, R. Wilson, T. Loriaux, J. Hernández, and A. Rivera, "50 MHz helicopter-borne radar data for determination of glacier thermal regime in the central Chilean Andes," *Ann. Glaciol.*, vol. 56, no. 70, pp. 193–201, 2015, doi: 10.3189/2015AoG70A953.

[7] F. Rodriguez-Morales *et al.*, "Advanced multifrequency radar instrumentation for polar research," *IEEE Trans. Geosci. Remote Sens.*, vol. 52, no. 5, pp. 2824–2842, May 2014, doi: 10.1109/TGRS.2013.2266415.

[8] L. S. Koenig *et al.*, "Wintertime storage of water in buried supraglacial lakes across the Greenland Ice Sheet," *Cryosphere*, vol. 9, no. 4, pp. 1333–1342, Jul. 2015, doi: 10.5194/tc-9-1333-2015.

[9] G. K. A. Oswald and S. P. Gogineni, "Recovery of subglacial water extent from Greenland radar survey data," *J. Glaciol.*, vol. 54, no. 184, pp. 94–106, 2008, doi: 10.3189/002214308784409107.

[10] D. M. Schroeder, D. D. Blankenship, and D. A. Young, "Evidence for a water system transition beneath Thwaites Glacier, West Antarctica," *Proc. Nat. Acad. Sci. United States Amer.*, vol. 110, no. 30, pp. 12225–12228, Jul. 2013, doi: 10.1073/pnas.1302828110.

[11] D. M. Schroeder, D. D. Blankenship, R. K. Raney, and C. Grima, "Estimating subglacial water geometry using radar bed echo specularity: Application to Thwaites Glacier, West Antarctica," *IEEE Geosci. Remote Sens. Lett.*, vol. 12, no. 3, pp. 443–447, Mar. 2015, doi: 10.1109/LGRS.2014.2337878.

[12] A. Rutishauser *et al.*, "Discovery of a hypersaline subglacial lake complex beneath Devon ice cap, Canadian Arctic," *Sci. Adv.*, vol. 4, no. 4, pp. 1–7, 2018, doi: 10.1126/sciadv.aar4353.

[13] H. Goelzer *et al.*, "The future sea-level contribution of the Greenland ice sheet: A multi-model ensemble study of ISMIP6," *Cryosphere*, vol. 14, no. 9, pp. 3071–3096, Sep. 2020, doi: 10.5194/tc-14-3071-2020.

[14] H. Seroussi *et al.*, "ISMIP6 Antarctica: A multi-model ensemble of the Antarctic ice sheet evolution over the 21st century," *Cryosphere*, vol. 14, no. 9, pp. 3033–3070, Sep. 2020, doi: 10.5194/tc-14-3033-2020.

[15] M. Morlighem *et al.*, "Deep glacial troughs and stabilizing ridges unveiled beneath the margins of the Antarctic ice sheet," *Nature Geosci.*, vol. 13, no. 2, pp. 132–137, Feb. 2020, doi: 10.1038/s41561-019-0510-8.

[16] A. G. Fountain and J. S. Walder, "Water flow through temperate glaciers," *Rev. Geophys.*, vol. 36, no. 3, pp. 299–328, 1998, doi: 10.1029/97RG03579.

[17] J. S. Bowling, S. J. Livingstone, A. J. Sole, and W. Chu, "Distribution and dynamics of Greenland subglacial lakes," *Nature Commun.*, vol. 10, no. 1, Dec. 2019, Art. no. 2810, doi: 10.1038/s41467-019-10821-w.

[18] A. Wright and M. Siegert, "A fourth inventory of Antarctic subglacial lakes," *Antarctic Sci.*, vol. 24, no. 6, pp. 659–664, Dec. 2012, doi: 10.1017/S095410201200048X.

[19] M. J. Siegert, N. Ross, and A. M. le Brocq, "Recent advances in understanding Antarctic subglacial lakes and hydrology," *Philos. Trans. Roy. Soc. A, Math., Phys. Eng. Sci.*, vol. 374, no. 2059, Jan. 2016, Art. no. 20140306, doi: 10.1098/rsta.2014.0306.

[20] G. E. Flowers, "Modelling water flow under glaciers and ice sheets," *Proc. Roy. Soc. A, Math., Phys. Eng. Sci.*, vol. 471, no. 2176, Apr. 2015, Art. no. 20140907, doi: 10.1098/rspa.2014.0907.

[21] H. Röthlisberger, "Water pressure in intra- and subglacial channels," *J. Glaciol.*, vol. 11, no. 62, pp. 177–203, 1972, doi: 10.3189/S0022143000022188.

[22] J. S. Walder and A. Fowler, "Channelized subglacial drainage over a deformable bed," *J. Glaciol.*, vol. 40, no. 134, pp. 3–15, 1994, doi: 10.3189/S0022143000003750.

[23] F. Gimbert, V. C. Tsai, J. M. Amundson, T. C. Bartholomaus, and J. I. Walter, "Subseasonal changes observed in subglacial channel pressure, size, and sediment transport," *Geophys. Res. Lett.*, vol. 43, no. 8, pp. 3786–3794, Apr. 2016, doi: 10.1002/2016GL068337.

[24] D. A. Young, D. M. Schroeder, D. D. Blankenship, S. D. Kempf, and E. Quartini, "The distribution of basal water between Antarctic subglacial lakes from radar sounding," *Philos. Trans. Roy. Soc. A, Math., Phys. Eng. Sci.*, vol. 374, no. 2059, Jan. 2016, Art. no. 20140297, doi: 10.1098/rsta.2014.0297.

[25] S. J. Radzevicius and J. J. Daniels, "Ground penetrating radar polarization and scattering from cylinders," *J. Appl. Geophys.*, vol. 45, pp. 111–125, 2000, doi: 10.1016/S0926-9851(00)00023-9.

[26] P. Lutz, S. Garambois, and H. Perroud, "Influence of antenna configurations for GPR survey: Information from polarization and amplitude versus offset measurements," *Geol. Soc. Special Publication*, vol. 211, pp. 299–313, 2003, doi: 10.1144/GSL.SP.2001.211.01.24.

[27] F. Lehmann, D. E. Boerner, K. Holliger, and A. G. Green, "Multicomponent georadar data: Some important implications for data acquisition and processing," *Geophysics*, vol. 65, no. 5, pp. 1542–1552, Jun. 2000, doi: 10.1190/1.1444842.

[28] A. P. Annan, "Electromagnetic principles of ground penetrating radar," in *Ground Penetrating Radar Theory and Applications*, H. Jol, Ed. Amsterdam, The Netherlands: Elsevier, 2009, pp. 1–544.

[29] C. A. Balanis, *Advanced Engineering Electromagnetics*, 2nd ed. Hoboken, NJ, USA: Wiley, 1989.

[30] M. E. Peters, D. D. Blankenship, and D. L. Morse, "Analysis techniques for coherent airborne radar sounding: Application to West Antarctic ice streams," *J. Geophys. Res., Solid Earth*, vol. 110, no. 6, pp. 1–17, Jun. 2005, doi: 10.1029/2004JB003222.

[31] N. D. Hargreaves, "The polarization of radio signals in the radio echo sounding of ice sheets," *J. Phys. D, Appl. Phys.*, vol. 10, pp. 1285–1304, 1977, doi: 10.1088/0022-3727/10/9/012.

[32] C. S. M. Doake, H. F. J. Corr, and A. Jenkins, "Polarization of radio waves transmitted through Antarctic ice shelves," *Ann. Glaciol.*, vol. 34, pp. 165–170, 2002, doi: 10.3189/172756402781817572.

[33] S. Fujita, H. Maeno, and K. Matsuoka, "Radio-wave depolarization and scattering within ice sheets: A matrix-based model to link radar and ice-core measurements and its application," *J. Gaciol.*, vol. 52, no. 178, pp. 407–424, 2006, doi: 10.3189/172756506781828548.

[34] J. Dall, "Polarimetric ice sounding at P-band: First results," in *Proc. Int. Geosci. Remote Sens. Symp.*, 2009, pp. 1024–1027, doi: 10.1109/IGARSS.2009.5418278.

[35] J. Dall, "Ice sheet anisotropy measured with polarimetric ice sounding radar," in *Proc. Int. Geosci. Remote Sens. Symp.*, 2010, pp. 2507–2510, doi: 10.1109/IGARSS.2010.5653528.

[36] R. Drews, O. Eisen, D. Steinhage, I. Weikusat, S. Kipfstuhl, and F. Wilhelms, "Potential mechanisms for anisotropy in ice-penetrating radar data," *J. Glaciol.*, vol. 58, no. 209, pp. 613–624, Jun. 2012, doi: 10.3189/2012JoG11J114.

[37] T. M. Jordan, D. M. Schroeder, D. Castelletti, J. Li, and J. Dall, "A polarimetric coherence method to determine ice crystal orientation fabric from radar sounding: Application to the NEEM ice core region," *IEEE Trans. Geosci. Remote Sens.*, vol. 57, no. 11, pp. 8641–8657, Nov. 2019, doi: 10.1109/TGRS.2019.2921980.
[38] T. M. Jordan, D. M. Schroeder, C. W. Elsworth, and M. R. Siegfried, "Estimation of ice fabric within Whillans ice stream using polarimetric phase-sensitive radar sounding," *Ann. Glaciol.*, vol. 61, no. 81, pp. 74–83, Apr. 2020, doi: 10.1017/aog.2020.6.
[39] K. Matsuoka, L. Wilen, S. P. Hurley, and C. F. Raymond, "Effects of birefringence within ice sheets on obliquely propagating radio waves," *IEEE Trans. Geosci. Remote Sens.*, vol. 47, no. 5, pp. 1429–1443, May 2009, doi: 10.1109/TGRS.2008.2005201.
[40] M. S. Haynes, "Surface and subsurface radar equations for radar sounders," *Ann. Glaciol.*, vol. 61, no. 81, pp. 135–142, Apr. 2020, doi: 10.1017/aog.2020.16.
[41] N. J. Cassidy, "Electrical and magnetic properties of rocks, solids and fluids," in *Ground Penetrating Radar Theory and Applications*, H. Jol, Ed. Amsterdam, The Netherlands: Elsevier, 2009, pp. 1–544.
[42] "Altair feko," Altair Engineering Inc., 2020.
[43] C. Warren, A. Giannopoulos, and I. Giannakis, "gprMax: Open source software to simulate electromagnetic wave propagation for ground penetrating radar," *Comput. Phys. Commun.*, vol. 209, pp. 163–170, Dec. 2016, doi: 10.1016/j.cpc.2016.08.020.
[44] F. T. Ulaby, R. K. Moore, and A. K. Fung, *Microwave Remote Sensing: Active and Passive*, 1st ed., Boston, MA, USA: Artech House, 1986.
[45] A. K. Fung and K. Chen, *Microwave Scattering and Emission Models for Users*. Boston, MA, USA: Artech House, 2009.
[46] J. A. Mikucki *et al.*, "Deep groundwater and potential subsurface habitats beneath an Antarctic dry valley," *Nature Commun.*, vol. 6, Apr. 2015, Art. no. 6831, doi: 10.1038/ncomms7831.
[47] J. D. Paden, C. T. Allen, S. Gogineni, K. C. Jezek, D. Dahl-Jensen, and L. B. Larsen, "Wideband measurements of ice sheet attenuation and basal scattering," *IEEE Geosci. Remote Sens. Lett.*, vol. 2, no. 2, pp. 164–168, Apr. 2005, doi: 10.1109/LGRS.2004.842474.
[48] T. M. Jordan *et al.*, "An ice-sheet-wide framework for englacial attenuation from ice-penetrating radar data," *Cryosphere*, vol. 10, no. 4, pp. 1547–1570, Jul. 2016, doi: 10.5194/tc-10-1547-2016.
[49] J. A. Macgregor *et al.*, "Radar attenuation and temperature within the Greenland ice sheet," *J. Geophys. Res. F, Earth Surf.*, vol. 120, no. 6, pp. 983–1008, 2015, doi: 10.1002/2014JF003418.
[50] M. E. Peters, D. D. Blankenship, S. P. Carter, S. D. Kempf, D. A. Young, and J. W. Holt, "Along-track focusing of airborne radar sounding data from West Antarctica for improving basal reflection analysis and layer detection," *IEEE Trans. Geosci. Remote Sens.*, vol. 45, no. 9, pp. 2725–2736, Sep. 2007, doi: 10.1109/TGRS.2007.897416.
[51] F. Hélière, C. C. Lin, H. Corr, and D. Vaughan, "Radio echo sounding of pine island glacier, West Antarctica: Aperture synthesis processing and analysis of feasibility from space," *IEEE Trans. Geosci. Remote Sens.*, vol. 45, no. 8, pp. 2573–2582, Aug. 2007, doi: 10.1109/TGRS.2007.897433.
[52] J. J. Legarsky, S. P. Gogineni, and T. L. Akins, "Focused synthetic aperture radar processing of ice-sounder data collected over the Greenland ice sheet," *IEEE Trans. Geosci. Remote Sens.*, vol. 39, no. 10, pp. 2109–2117, Oct. 2001, doi: 10.1109/36.957274.

Kirk M. Scanlan received the B.S. degree in geophysics from the Western University, London, ON, Canada, in 2011, the M.A.E.S. degree in applied geophysics from the TU Delft, Delft, The Netherlands, the M.S. degree in applied geophysics from the ETH Zurich, Zurich, Switzerland, the M.S. degree in applied geophysics from the RWTH Aachen, Aachen, Germany, in 2013, and the Ph.D. degree in geotechnical engineering from the University of Alberta, Edmonton, AB, Canada, in 2018.

He is currently a Postdoctoral Fellow with the DTU Space, Technical University of Denmark, Kongens Lyngby, Denmark. He is an affiliate of the Europa Clipper science team associated with the Radar for Europa Assessment and Sounding: Ocean to Near-Surface instrument. His research interests include radar signal processing, radar sounding of planetary bodies and cryospheres, and the intersection of near-surface geophysics and geotechnical engineering.

Dillon P. Buhl (Member, IEEE) received the B.S. and M.S.E. degrees in electric engineering from the University of Texas at Austin, Austin, TX, USA, in 2001 and 2004, respectively.

He is currently a Research Engineering Associate with the University of Texas Institute for Geophysics, Austin, TX, USA. He is also an affiliate of the Jet Propulsion Laboratory working on the Radar for Europa Assessment and Sounding: Ocean to Near-Surface instrument aboard the Europa Clipper mission. His research interests include antenna design and radar development and has participated in six polar aerogeophysical research expeditions.

Donald D. Blankenship received the B.S. degree in geology from the Eastern Illinois University, Charleston, IL, USA, in 1978, and the M.S. and Ph.D. degrees in geophysics from the University of Wisconsin, Madison, WI, USA, in 1982 and 1989, respectively.

He is currently a Senior Research Scientist with the Institute for Geophysics, Jackson School of Geosciences, University of Texas at Austin, Austin, TX, USA. He has been the funded PI or Co-PI on more than 30 data acquisition and analysis projects. He has more than 25 years of experience leading airborne and ground-based field campaigns in Antarctica and was the Chief Scientist and PI for all U.S. National Antarctic Aerogeophysics, from 1994 to 2002. He is also the PI on the Radar for Europa Assessment and Sounding: Ocean to Near-surface on NASA's Europa Clipper mission. His research interests include understanding earth's ice sheets and the underlying lithosphere through coupled geophysical observations, as well as planetary studies involving radar sounding investigations.

Dr. Blankenship is a member of the American Geophysical Union.